Journal Pre-proof

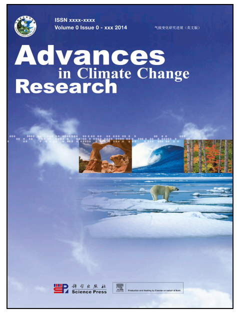

Assessing the impact of artificial geotextile covers on glacier mass balance and energy fluxes

Yi-Da XIE, Fei-Teng WANG, Hui ZHANG, Wen-Tao DU, Wei-Bo ZHAO

PII: S1674-9278(24)00157-6

DOI: https://doi.org/10.1016/j.accre.2024.10.007

Reference: ACCRE 574

To appear in: *Advances in Climate Change Research*

Received Date: 26 March 2024

Revised Date: 28 July 2024

Accepted Date: 24 October 2024

Assessing the impact of artificial geotextile covers on glacier mass balance and energy fluxes

Yi-Da XIE[a,b], Fei-Teng WANG[a *], Hui ZHANG[a], Wen-Tao DU[a], Wei-Bo ZHAO[a,b]

[a] *Key Laboratory of Cryospheric Science and Frozen Soil Engineering, Northwest Institute of Eco-Environment and Resources, Chinese Academy of Sciences, Lanzhou 730000, China*

[b] *University of Chinese Academy of Sciences, Beijing 100049, China*

Abstract As global warming accelerates, leading to the retreat of glaciers, the effectiveness of artificial coverings, in particular geotextiles, in reducing glacier ablation has emerged as a topic of increasing concern. Nevertheless, a critical gap in knowledge persists regarding the specific physical processes involved in the mitigation provided by these coverings. This study explores the underlying mechanisms that govern the interaction through field observations and COSIPY model simulations at Bailanghe Glacier No. 21 in the Qilian Mountains from 26 June to 17 September 2023. It compares covered and uncovered areas to evaluate differences in mass and energy balance fluxes. It was discovered that geotextiles could decrease ice melt by up to 1000 mm w.e. in comparison to the surface of glaciers without cover, primarily because of a 23% increase in albedo compared to ice, leading to a decrease in net short-wave radiation and available melt energy. The effect of covering the entire glacier with a geotextile, which has varying albedo properties, was also simulated. It was found that, with every 5% increase in the albedo of the geotextile, ablation was reduced by 10%–25%, resulting in a decrease in ice volume loss of approximately 2.5×10^5 m^3. While artificially covering glaciers can reduce ablation rates, it faces challenges such as high costs, environmental risks, and issues with replicability. Ultimately, this study aims to analyze the feasibility of glacier coverage from a mechanistic perspective for glacier management amidst ongoing climate change.

Keywords: Artificial coverings; Mass and energy balance; COSIPY model; Qilian Mountains; Bailanghe Glacier No.12

1. Introduction

Glaciers worldwide have been thinning at an accelerated pace since the beginning of the 21st century (Gardner et al., 2013; Dehecq et al., 2019), with a mean mass balance of −0.42 m w.e. per year (Burn et al., 2017). The glaciers on the Tibetan Plateau and surrounding ranges, known as High Mountain Asia (HMA), serve as the Asian water tower, offering the most abundant glacier resources outside the polar regions (Pritchard et al., 2019; Bhattacharya et al., 2021). However, the majority of these glaciers are undergoing remarkable shrinkage and becoming increasingly vulnerable due to continuous climate warming (Yao et al., 2022; Zhao et al., 2022). Under scenarios involving high greenhouse gas emissions, it is predicted that glaciers will almost completely disappear in many areas (Farinotti et al., 2019). As a consequence of these changes, alterations in river flow are anticipated, impacting cryosphere-related hazards, regional ecosystems, socio-economic activities, and the culture and tourism associated with glaciers and human societies (Huss and Hock, 2018).

To address this existential challenge, researchers have attempted to develop innovative and effective methods for snow and ice protection, especially for alpine glacier ski resorts (Spandre et al., 2016). Glaciers in the Alpine region are indisputably key economic contributors, attracting tourists with their captivating beauty, and their diminishing presence adversely affects the viability and profitability of ski resorts in the European Alps (Fischer et al., 2016). In light of this, since the early 2000s, remarkable efforts have been made to develop methods to artificially decelerate snow and ice melt in order to preserve glacier surface elevation as required (Olefs and Fischer, 2008). The majority of these techniques focused on either enhancing albedo or reducing thermal conductivity to diminish the energy available for melting the underlying snow or ice (Senese et al., 2020). Wang et al. (2018) explored the impact of artificial snowfall on the mass balance of Muz Taw Glacier (Sawir Mountains, China) on 19 and 22 August 2018, finding an increase in mass balance of between 32–41 mm w.e. Moreover, several studies have shown that covering glaciers with geotextiles greatly affects their mass balance during the ablation period (Wang et al., 2023; Huss et al., 2021). For example, during the 2004–2005 ablation period, the Schaufelferner and Gaißkarferner glaciers were covered with various types of geotextiles (Olefs and Fischer, 2008). The results demonstrated that a 0.004 m thin cover material greatly improved the glaciers' mass balance, reducing the melting rate and total ablation by 60%. In Switzerland, active coverage of glaciers using geotextiles has been achieved at nine sites for up to 15 years, covering an area of 0.18 ± 0.01 km² by 2019. This technique mitigates up to 350,000 m^3 of ice melt per year, preserving an average of 2 m of ice annually in the covered area (Huss et al., 2021). Until 2018, a comprehensive scientific assessment of active glacier protection strategies in China had not been conducted. Since then, three experiments involving non-woven geotextiles have been carried out in different regions, including Urumqi Glacier No. 1 and Dagu Glacier No.17 in summer, revealing through observation that geotextiles with higher albedo than bare ice can effectively reduce glacier ablation. (Xie et al., 2023; Wang et al., 2023). Despite the practical success of these initiatives during ablation period, most studies focused primarily on the protective effect of the cover material and the radiation balance recorded by weather stations. The knowledge gap remains regarding the precise physical processes that govern the application of geotextiles to snow and ice cover.

This study is based on data from automatic weather stations (AWS) of Bailanghe Glacier No.21 (BLH), used as input for a process-oriented adaptation of an open-source coupled snowpack and ice surface energy and mass balance model (COSIPY) (Sauter et al., 2020). In order to characterize in detail the process of mass and energy transport transformations of geotextile-covered snow and ice surfaces, we investigated mass balance management by using geotextiles covering glaciers from June 26 to September 19, 2023. Specifically, this study aims to: 1) compare the effects of geotextiles covering glacier mass balance change patterns in covered and uncovered areas by applying high-resolution digital elevation models (DEMs) and *in-situ* measurements; 2) apply the

COSIPY model to simulate changes in glacier mass balance, energy fluxes, and ice volume utilizing AWS data within both covered and uncovered areas to assess and quantify the mass and energy transport transformations under different covering conditions. This study enhances our understanding of the mechanisms by which geotextiles modulate energy and mass balance, highlighting their significant potential and limitation to mitigate glacier melt in the background of climate change.

2. Study area

The BLH (38°56.8′N, 99°17.2′E), located on the northern slope of the middle part of the Qilian Mountain Nature Reserve (Fig. 1), covers an area of 1.45 km^2 and has a length of 2.5 km (Chen et al., 2023). The glacier flows in a northeastward direction from elevations of 4290–5103 m a.s.l. Chen (2023) reported that the average mass balance of the BLH was –534 ±166 mm w.e. in 2020–2021. On the basis of glacial meteorological data, the temperature mostly surpasses 0 °C from May to September, and the average temperature is –7.4 °C. Furthermore, the annual precipitation total of the BLH is 568.7 mm in 2020–2021, which occurs mainly from April to August, accounting for 80.6% of the annual precipitation. The prevailing weather conditions are characterized by a predominance of cloudy skies. In terms of short-wave radiation, the highest monthly incident and reflected radiation levels are observed in May and April, respectively.

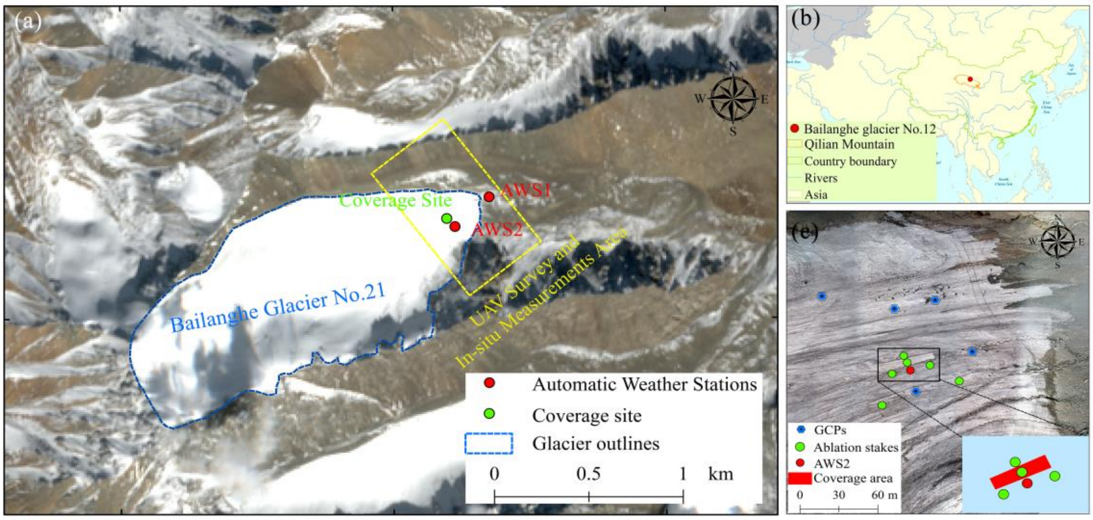

Fig. 1. (a) Overview of the BLH, including the unmanned aerial vehicle (UAV) survey areas and *in-situ* measurement area, coverage area, automatic weather stations, and glacier outlines (the background image is a Sentinel_2A false color image on 2 October 2023), and (b) UAV-derived three-dimensional images of the glacier, the details of the coverage area, the measuring sites and ground control points (GCPs) for mass balance on the BLH.

3. Data and methods

3.1 Field observations and installation

In the selected area, annual point surface mass balances were monitored using five ablation stakes, which were positioned at elevations corresponding to AWS2 and the coverage area. These stakes, 6 m in length, are composed of six 1-m-long iron bars (Fig. 2d). Four ablation stakes were installed around the covered area on 26 June 2023, and an additional two stakes were added one week later to complete the mass-balance observation network in the experimental area. Detailed observations were conducted unscheduled from 26 June to 19 September, 2023, throughout the entire trial period. These observations included measuring the vertical height of the stakes above the glacier surface and determining the thickness and density of each snow/ice layer. The mean mass balance uncertainty measured was ±0.2 m w.e. per year, excluding the effect of system factors (Zemp et al., 2010). Specifically, the mass balance from field measurements is utilized to assess the coverage effectiveness and to validate the model simulations between covered and uncovered areas.

Hourly meteorological data were used to drive the COSIPY model for the simulation of covered and uncovered areas. Two AWSs were critical for comprehensive meteorological data collection: AWS1, installed at the glacier terminus in 2020, and AWS2, installed in June 2023 at the edge of the experimental site (Fig. 1). AWS1 records air temperature, relative humidity, precipitation, wind speed, wind direction, air pressure, as well as short-wave and long-wave radiation components. The meteorological elements used have undergone rigorous quality control procedures to ensure the absence of outliers for temperature, relative humidity, air pressure, long-wave incoming radiation, short-wave incoming radiation, and precipitation. Additionally, AWS2 was equipped with two four-component net radiation systems (CRN4), primarily used for measuring the short-wave and long-wave reflectivity of ice and associated materials (Fig. 2c). Due to the complex meteorological environment on the ice surface, AWS data may exhibit gaps. To address this issue, AWS1 and AWS2 data were mutually complementary for corresponding time periods, ensuring a continuous meteorological dataset. COSIPY is optimized with observations from the two AWSs, especially in terms of ice albedo.

Late June to early September marks the end of the summer melt and the beginning of winter accumulation, a crucial period since snow contributes to glacier accumulation, mitigating the rate of glacier melting (Wang et al., 2019). Covering the glacier during this period does not compromise the protective impact of snow on the glacier. The cover material is a non-woven fabric (geotextile) made of UV-stabilized polypropylene fibers, known for its high tensile strength and short-wave reflectivity. Ideally, the cover is placed on the glacier surface before the start of the summer ablation period. At the end of the ablation period, the covers are recycled to ensure the material's reuse. In practice, rolls of geotextile (50 m × 6 m) are transported by hand to the glacier surface and secured with ropes and bags. Placing the cover directly on the snow or ice surface influences the energy balance of the underlying snow surface, reducing the amount of energy available for melting (Fig. 2a). Ultimately, the geotextile was deployed over a 300 m^2 experimental field (Fig. 2b) from 26 June to 17 September 2023.

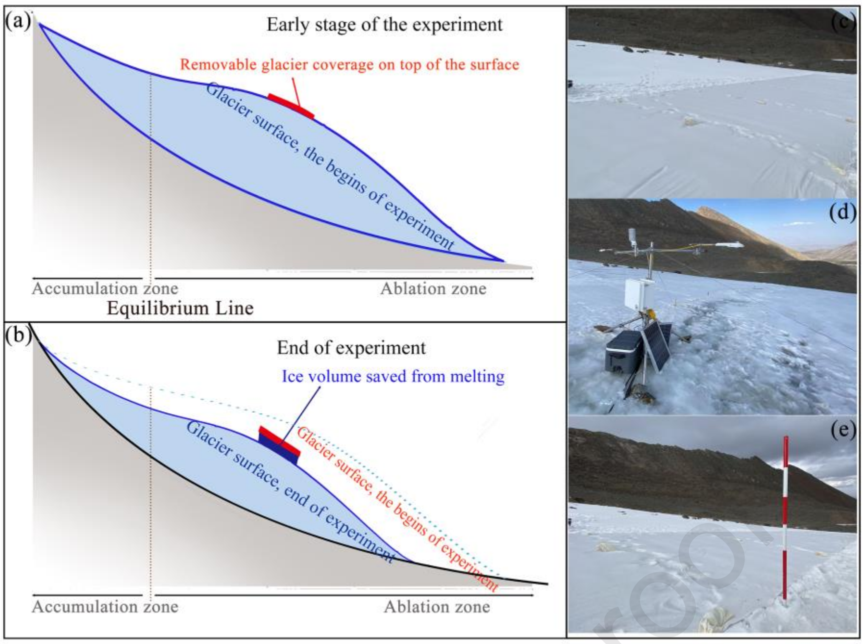

Fig. 2. Schematic diagrams of the early stage (a) and end (b) of the experiment of artificial cover in the ablation zone to reduce glacier melt (refer to Huss et al., 2021), (c) overview of the geotextile cover, (d) AWS2, and (e) ablation stake.

3.2 UAV flights and data processing

To perform high-precision observations, a DJI Phantom 4 Real-Time Kinematic (RTK) UAV was flown twice, connecting to the network RTK; initially on 26 June 2023, coinciding with the laying of the geotextile fabric and installation of the meteorological station, and subsequently on 17 September 2023. Two UAV surveys with high overlap were conducted between June–September 2023, yielding raw images with higher ground sampling distances (GSD). The details of the UAV survey-related information are in Table 1. The images captured during each UAV survey were post-processed using structure-from-motion and multi-view-stereo (SfM-MVS) techniques. The Pix4D Mapper software was chosen for the experiments because of its ability to quickly process the images and reconstruct DEMs and Ortho-mosaics with high quality.

Table 1. Details of the UAV coverage area and flight-related information.

Parameter	26 June 2023	17 September 2023
Coverage (km^2)	0.259	0.073
Flight type	RTK	RTK

Flight altitude (m)	190	155
Ground resolution (cm)	3.9	1.7
Number of photos taken/valid photos	186/193	188/193
Number of checkpoints used	5	5
Flight time (Beijing time)	14:43–15:18	13:55–14:14

Accuracy traditionally relies on ground control points (GCPs; Qiao et al., 2023; Martínez-Carricondo et al., 2018). Five square ground reflective targets (1 m × 1 m) were installed on the survey areas of the BLH as GCPs (Fig. 1c). These GCPs were measured before the flight in RTK mode using a global navigation satellite system (GNSS) receiver, with the base station located within the glacier terminus. Five ground validation points were established on the BLH surface to determine the accuracy of the UAV-derived outputs (Fig. 1a), coinciding with the UAV surveys, whose absolute geolocation accuracy were measured using GNSS (Table 2).

Table 2. Absolute geolocation accuracy differences between ground ground validation points and UAV-derived DEM.

Date	*X* (m)	*Y* (m)	*Z* (m)
26 June 2023	0.09	0.07	0.12
17 September 2023	0.04	0.03	0.08

3.3 COSIPY model

COSIPY combines a surface energy balance with a multilayer subsurface snow and ice model to compute the glacier mass balance. The surface energy balance can be written as follows:

$$Q_{\mathrm{M}} = S_{\mathrm{in}}(1-\alpha) + L_{\mathrm{in}} + L_{\mathrm{out}} + Q_{\mathrm{sens}} + Q_{\mathrm{lat}} + Q_{\mathrm{G}} \quad (1)$$

where Q_{M} represents the energy available for melting, S_{in} is the incoming short-wave radiation, α denotes albedo, L_{in} is the incoming long-wave radiation, L_{out} refers to the outgoing long-wave radiation, Q_{sens} stands for the sensible heat flux, Q_{lat} represents the latent heat flux, and Q_{G} denotes the glacier heat flux. In COSIPY, S_{in} is computed using radiation model, which calculates clear-sky shortwave radiation based on geographical and topographical factors (Kumar et al., 1997). The radiation model operates using the SRTM DEM (30 m). Energy fluxes towards the surface are positive, and ablation occurs via sublimation, subsurface melt, and surface melt, with surface melt requiring the surface temperature (T_s) to be at 273.15 K and positive energy flux (Q_M). COSIPY uses meteorological data to compute atmospheric energy fluxes and the subsurface temperature profile to determine Q_G. Q_M and Q_{lat} are converted to mass fluxes, contributing to the MB at the glacier surface. T_s is crucial for calculating L_{out}, Q_{sens}, Q_{lat}, and Q_G, and its iterative calculation ensures energy equilibrium at the surface. If T_s exceeds 273.15 K, it is reset, and the residual energy flux Q_M equals the energy available for surface melting (Q_{melt}) (Sauter et al., 2020). All snowfall on the ice surface brings mass accumulation to the glacier because the sublimation processes of fresh snow and firn are not calculated. The separation of rain and snow is achieved using a logistic transfer function, and the proportion of solid precipitation typically varies smoothly between 100% (0 °C) and 0% (2 °C) (Hantel et al., 2000). To achieve optimal simulation performance of COSIPY in the BLH setting, parameter optimization is required. The final key parameterizations and parameter selections refer to Mölg et al. (2012), Arndt and Schneider (2023), Potocki et al. (2022), and Blau et al. (2021). The albedo of the ice is based on the empirical data collected by AWS2.

4. Results

4.1 Microclimatic conditions on the glacier surface

The main data required in the energy–mass balance model were meteorological data, which are often representative of one station in the study region. The hour-by-hour meteorological data from which the daily average data are also derived serve as input data for the COSIPY model (Fig. 3). Thus, hourly meteorological data were input into the model to simulate the mass balance of the BLH between 26 June and 17 September. Throughout the experimental period, relative humidity was consistently high, with an average of 68% (Fig. 3a). A gentle breeze was observed on average across the glacier, with a mean wind speed of 2.14 m s^{-1} (Fig. 3b). L_{in} was highly variable, with a mean of 275.32 W m^{-2} (Fig. 3c). S_{in} played a crucial role as a model forcing factor. Daily variations in S_{in} ranged from 26–411 W m^{-2} due to fluctuating cloud cover, with values varying approximately from 600 W m^{-2} during the day to 200 W m^{-2} at night, resulting in an average value of 220 W m^{-2} (Fig. 3d). The total precipitation recorded throughout the period with complete data was 203 mm (Fig. 3e), of which 84 mm was classified as snowfall (Mölg et al., 2012; Ageta and Fujita, 2000). The hourly mean air temperature was around 3 °C for the duration of the experiment. The range of mean daily air temperatures varied from −1.07 to 7.93 °C, with temperatures almost always remaining above the melting point (Fig. 3f). Daily mean observed temperature lapse rate values were calculated using linear regression of the daily air temperatures, showing a variability of −0.03 °C d^{-1}. Pressure remained relatively stable throughout the experimental period, with an average value of 625 hPa (Fig. 3g).

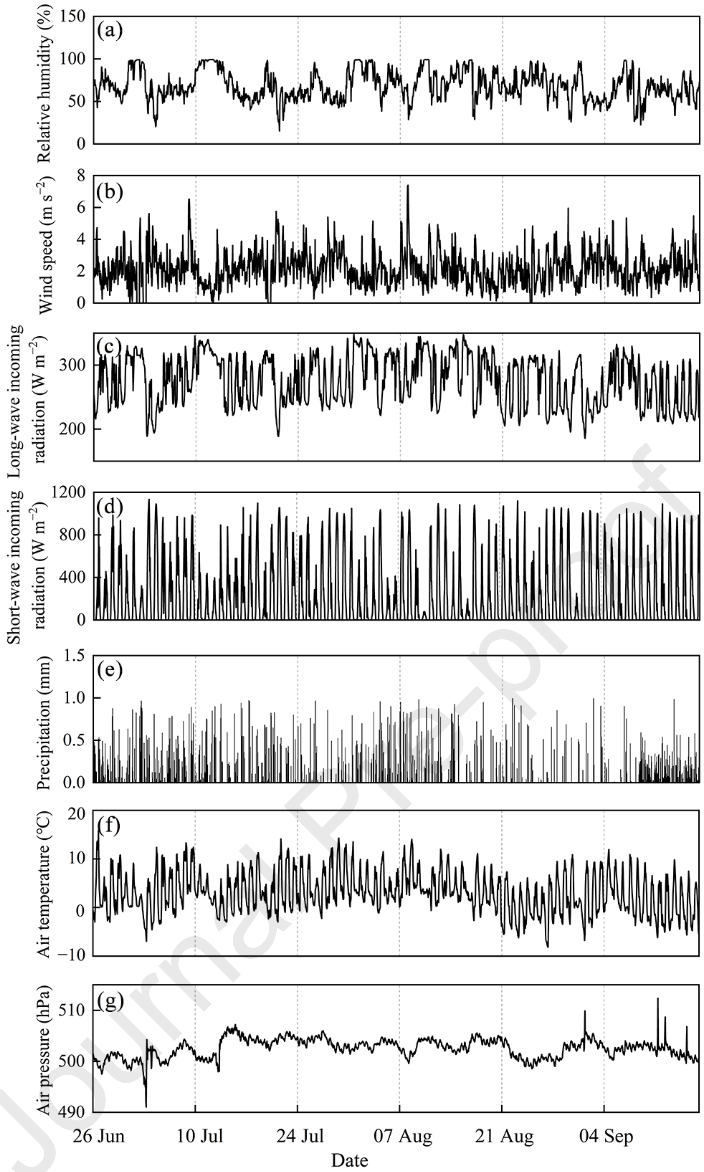

Fig. 3. Hourly means of meteorological variables at the BLH from 26 June to 17 September 2023 showing (a) relative humidity, (b) wind speed, (c) long-wave incoming radiation, (d) short-wave incoming radiation, (e) precipitation, (f) air temperature, and (g) air pressure.

4.2 Observed and simulated energy fluxes in covered and uncovered areas

The model simulations are satisfactory and offer an accurate depiction of the energy fluxes' inflow and outflow. Fig. 4 presents the average daily surface energy fluxes near the AWSs in the BLH experimental area from June–September 2023. The net energy flux directed toward the glacier was converted into daily melt rates in ice equivalent, utilizing an ice density of 917 kg m^{-3} (Schaefer et al., 2020). For BLH, the primary energy contribution was from net short-wave radiation (S_{net}: average +130 W m^{-2}), as during the summer S_{net} on a glacier constitutes a portion of the surface energy balance, frequently comprising 75% or more of the energy available at the surface (Olson and Rupper, 2019). This was followed by the Q_{sens} (average +5.46 W m^{-2}), indicating that the air temperature 2 m above the glacier is higher than that of the glacier surface, thereby transferring energy to the glacier surface, and the Q_{G} (average +4.71 W m^{-2}). Alternatively, the mean values of the shares of S_{net}, Q_{sens} and Q_{G} in the energy income term of the glacier surface during the experimental period were 93%, 4%, and 3%, respectively, with S_{net} being the main source of energy input at the glacier surface. The daily average value of Q_{lat} (average −2.21 W m^{-2}) was consistently negative, indicating that the specific humidity of the air was lower than that of the glacier surface, resulting in the transfer of heat from the glacier surface to the atmosphere in the form of latent heat (Mölg et al., 2012). Net long-wave radiation (L_{net}) acted as a heat sink (average −26.70 W m^{-2}). Most of the surface energy was utilized for melting surface snow/ice melting (average −91.98 W m^{-2}).

In the covered area, the individual energy fluxes differed greatly. The S_{net} at the covered area showed strong day-to-day variability, fluctuating between 9–151 W m^{-2} (on average +80.09 W m^{-2}). The average S_{net} at the covered area was 50 W m^{-2} than in the uncovered area, while the values of Q_{sens} (on average +5.57 W m^{-2}) and Q_{G} (on average +3.24 W m^{-2}) in the covered area were roughly equivalent to those in the uncovered area (Fig. 4). The mean contributions of S_{net}, Q_{sens} and Q_{G} in the energy income term of the glacier surface during the experimental period were 90%, 6%, and 4%, respectively. Generally, the net long-wave radiation (L_{net}) was negative in the covered area, with an average value of –25.45 W m^{-2}, indicating a negative impact of long-wave radiation on glacier melting. This area is similar to the uncovered area in that most of the surface energy is used for surface snow/ice melt, with a mean value of −49.93 W m^{-2}. In contrast to Q_{melt} and L_{net}, the Q_{lat} turbulent fluxes in the glacier cove area were small, at only −1.51 W m^{-2}. The results of comparing the simulations for each energy flux show that the covered area has a reduction in energy income of approximately 52 W m^{-2}. Specifically, S_{net} decreased by approximately 51 W m^{-2}, and Q_G decreased by nearly 1.5 W m^{-2}. Compared with the uncovered area, the covered area had a 37% reduction in energy income, but S_{net} was still the dominant energy income. On the energy output side, Q_{melt} was reduced by 42 W m^{-2}, L_{net} by 1.2 W m^{-2}, and Q_{lat} by 0.7 W m^{-2}. Q_{melt} was greatly reduced by 46%.

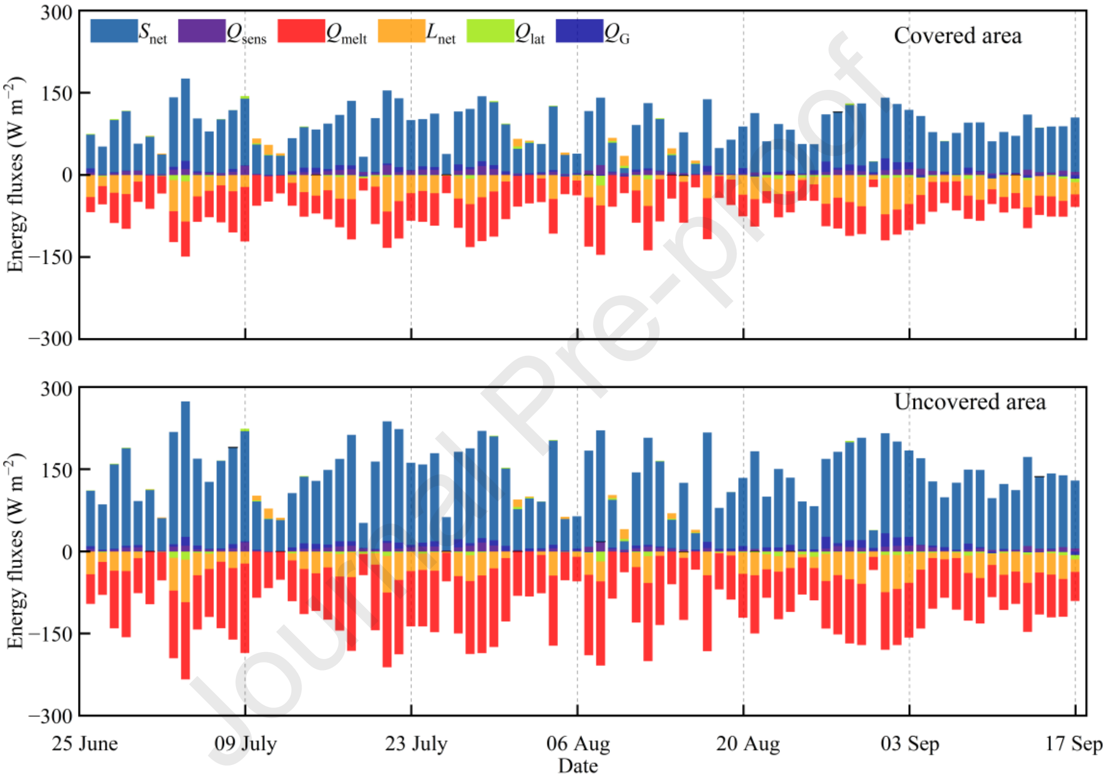

Fig. 4. Daily energy components of the BLH in the covered and uncovered areas from 26 June to 17 September 2023.

4.3 Spatial and temporal changes in observed and modeled glacier mass balance

Up to the final stage of the experiment, the elevation of the covered area was greater than that of the uncovered area, as shown on the topographic map of the BLH terminal and the partial profile of the covered area (Fig. 6). The elevation of the covered area is greater than that of the uncovered area, which is approximately 1 m greater. For example, the uncovered area in the middle section of the covered area in the right panel of Fig. 5a is mostly located at 4356–4357 m a.s.l., while the elevation of the S1–S2 section is mostly greater than 4358 m a.s.l. The elevation of the covered area is approximately 1 m greater than that of the uncovered area in the right panel of Fig. 6a, indicating greater glacier thickness in the covered area. Fig. 5b shows the multi-period DEM obtained via repeated photogrammetry to examine changes in glacier thickness within the BLH experimental area and to objectively evaluate the effectiveness of textile materials in glacier protection. The results reveal that in the uncovered areas, elevation changes mainly vary from –3 to –1.5 m, with some regions undergoing changes between –4 to –3 m and −2 to –1 m. In contrast, elevation changes in the areas covered by textile materials are less severe, generally ranging from –1.5 to –1 m.

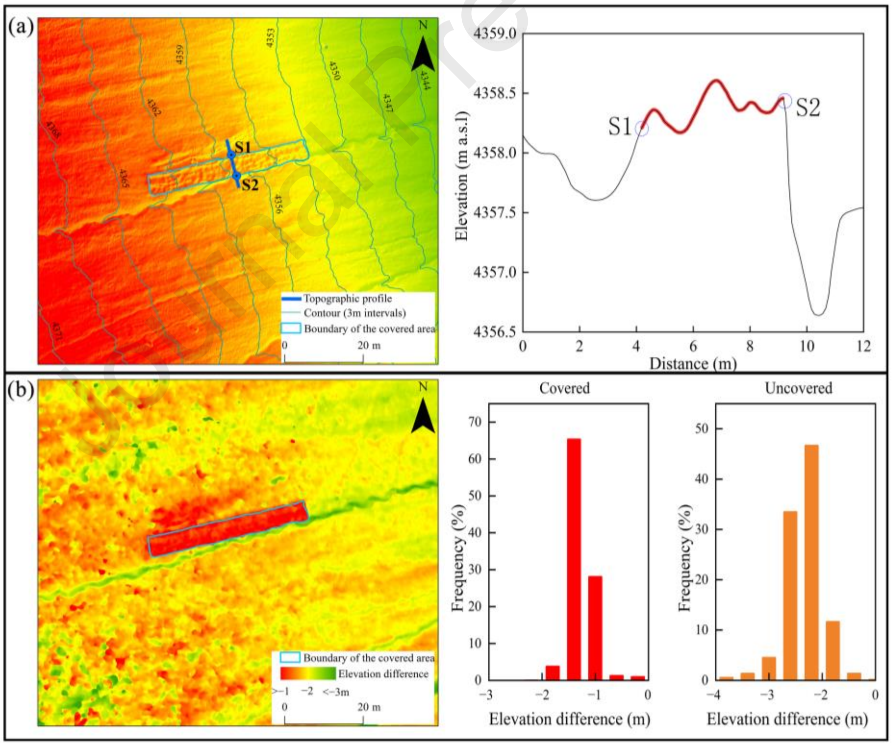

Fig. 5. UAV high-resolution image maps of covered and uncovered areas and their derived data, (a) topographic map of the BLH coverage test area (The background image is a digital elevation model (DEM) acquired by a UAV on 17 September 2023) and the profile topography of the blue line portion, and (b) the surface elevation change statistics for the experimental periods and the corresponding frequency distribution.

The modeled and measured mass balances were in agreement throughout the experiment, as illustrated in Fig. 6. The experimental period showed a consistent decrease in glacier mass balance, with the exception of night frosts, during which all available heat was dedicated to raising the glacier surface temperature to the melting point. Fig. 6 displays the melt rates inferred from COSIPY model simulations. The net energy flux reaching the glacier was converted into a daily melt rate equivalent to ice, using an ice density of 917 kg m^{-3}. During 26 June to 17 September 2023, the simulation indicated a mass balance (ablation) for the covered area of −1052 mm w.e. (−12.5 mm w.e. d^{-1}). Ablation was marginally higher in the initial period (26 June to 6 August) compared to the latter period (7 August to 17 September), with totals of 568 and 484 mm w.e., accounting for 54% and 46% of the total ablation, respectively. The average daily ablation difference between July and August was 14%, with rates of 14 and 12 mm w.e. d^{-1}, respectively. Nighttime ablation rates varied from 0–0.6 mm w.e., while daytime rates ranged from 0–4.5 mm w.e. Over the same period, the simulated total ablation in the uncovered area was 2029 mm w.e., or 24.2 mm w.e. d^{-1}. Snowfall and refreezing processes contributed to an accumulation of 48 mm w.e., mainly occurring at night.

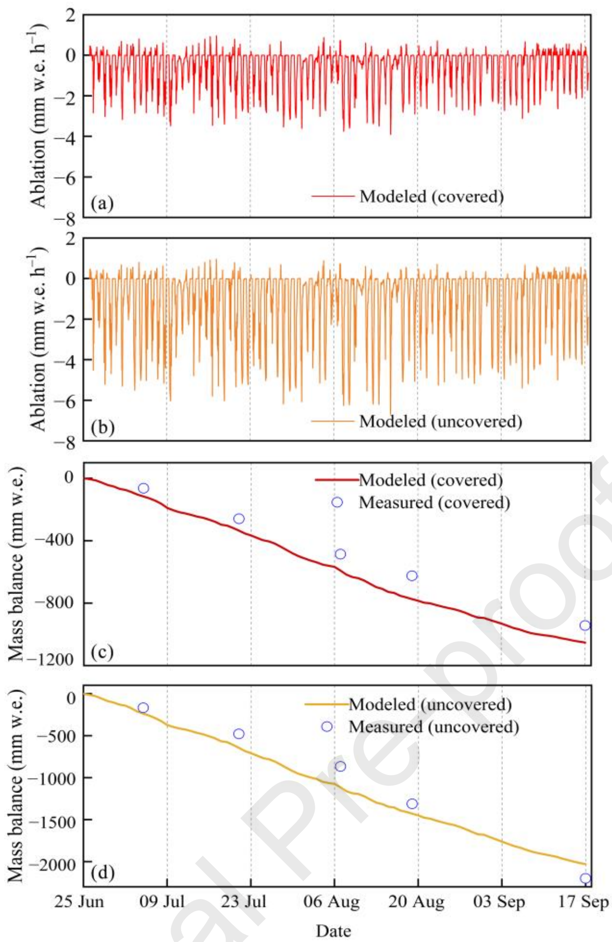

Fig. 6. Modeled hourly scale changes in mass balance for covered (a) and uncovered areas (b), and modeled (c) and measured (d) daily scale changes in mass balance from 26 June to 17 September 2023.

5. Discussion

5.1 Uncertainty assessment and validation

The primary sources of uncertainty stem from errors in UAV positioning and model simulations. By comparing ground validation point measurements with UAV-derived Ortho-mosaics and DEMs, we determined the absolute *XYZ* accuracies of the UAV-SfM survey product as presented in Table 2. The uncertainties in UAV measurements, analyzed as the mean absolute deviation in the *X*, *Y*, and *Z* directions, are 0.09 and 0.04 m, 0.07 and 0.03 m, and 0.12 and 0.08 m, respectively (Table 2). Notably, the vertical uncertainty is double that of the horizontal uncertainty, corroborating other findings (James et al., 2017; Zhao et al., 2023). Further, when comparing model simulation with measured data, it was observed that the model slightly overestimated the total ablation, with a root mean square error (RMSE) of the mass balance in the uncovered area of 165 mm w.e., while the simulated RMSE of the mass balance in the covered area was 103 mm w.e. At the experiment's conclusion, the modeled mass balance in the uncovered area (–2029.34 mm w.e.) exceeded the measured mass balance by 170 mm w.e.; conversely, the modeled mass balance in the covered area (–1051.80 mm w.e.) was 108 mm w.e. lower than the measured mass balance. The comparison between measured and modeled mass balances reveals correlation coefficients above 0.95 for both covered and uncovered areas. The notable disparity between modeled and measured ablation in the covered area can be attributed to the mitigating effect of summer snowfall on surface melting (Yang et al., 2011). Regarding the simulation outcomes for the uncovered area, the discrepancy primarily arises from the use of measured albedo parameters, which may not accurately reflect the albedo across the entire glacier terminus, suggesting that an underestimation of albedo contributed to the difference between simulated and measured results. In summary, the discrepancies observed between UAV-SfM survey comparisons and model simulations relative to measured data fall within acceptable limits.

5.2 The mechanism of action of artificial coverage

Multi-scale interactions between the glacier surface and the overlying atmosphere greatly affects various energy fluxes at glacier surfaces (Mott et al., 2020). The difference in energy gain or loss compared to the uncovered area may be attributed to the covered area reducing glacier ablation by nearly 1000 mm w.e., leading to a 12 mm w.e. d^{-1} deceleration in the melt rate. As illustrated in Fig. 3, with an average air temperature of 3 °C in the glacier area during the testing period, the temperature remained above the melting point approximately 75% of the time; thus, accelerating the glacier melt rate. S_{net} acts as the primary energy source for glacier melting, with an average incident short-wave radiation value of 220 W m^{-2} during the experimental period. However, there is a slight discrepancy between the S_{net} values of the covered and uncovered areas, with a difference of +50 W m^{-2}. L_{net} is predominantly negative, with values around −26 W m^{-2} for both the covered and uncovered areas. The absorbed heat is mainly used for melting and evaporation/sublimation processes (Osipov and Osipova, 2021). Other energy components such as Q_{sens}, Q_{G}, and Q_{lat}, exhibit minimal variation between the simulation results with and without geotextile cover, as indicated in Table 3. This minimal variation is primarily because the impact of the geotextile on increasing the ice surface albedo surpasses its thermal insulation properties. Given that the geotextile is only 0.5 mm thick, its main function is to enhance the ice surface's ability to reflect short-wave radiation. A decreased albedo on the glacier surface leads to weakened reflection of short-wave radiation, thereby accelerating glacier ablation (Zhang et al., 2020; Naegeli and Huss, 2017). Conversely, increasing glacier surface albedo leads to weakening of shortwave absorption and net radiation, further affecting the mass balance of the glacier.

Fig. 7 comprehensively depicts the recorded albedo changes between the glacier and geotextile surfaces throughout the experiment, utilizing meteorological instruments. The albedo of the geotextile was greatly higher than that of the glacier surface, with the geotextile's albedo showing greater fluctuations, ranging from 0.5–0.8. This variability was mainly due to snowfall deposition, which led to substantial changes in surface albedo (de Vrese et al., 2021). On the other hand, the glacier surface's albedo remained relatively stable, fluctuating between 0.3–0.55. Both surfaces showed a decreasing trend in albedo values, with the geotextile decreasing from about 0.8–0.5 and the glacier surface from 0.55 to 0.35 (Fig. 7). The decline in the geotextile's albedo is primarily attributed to factors such as snow and ice erosion, microorganisms, chemical agents, and various environmental conditions (Senese et al., 2020). Conversely, the changes in the glacier surface's albedo are mainly due to wind erosion in the valley, atmospheric deposition, and gradual accumulation of light-absorbing materials (Williamson and

Menounos, 2021; Kang et al., 2020). Nonetheless, the geotextile's albedo was consistently higher than that of the ice surface during the covering period. The higher albedo of the geotextile contributed to reducing the energy absorbed by the ice surface, thereby diminishing the energy available for melting. The energy consumed for melting in the uncovered area (91.98 W m^{-2}) was higher than that in the covered area (49.93 W m^{-2}) by 42 W m^{-2}. However, this experiment focused exclusively on monitoring the albedo parameter, without a detailed investigation into the ice surface temperature or the geotextile's thermal insulation effect, which suggests the need for further research in these areas.

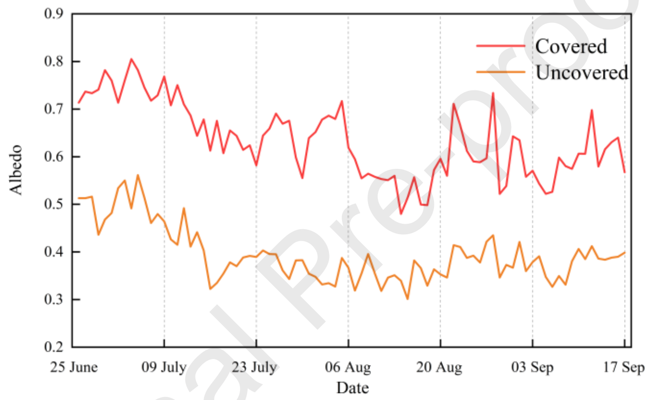

Fig. 7. Short-wave albedo changes on geotextiles and glacier surfaces from 26 June to 17 September, 2023.

Table 3. Comparison of simulated average energy components for geotextile-covered and geotextile-uncovered areas with different albedo performances.

Type		Energy flux (W m^{-2})					
		S_{net}	Q_{sens}	Q_G	Q_{melt}	L_{net}	Q_{lat}
Experiment	Covered	80.09	5.57	3.24	−49.93	−25.45	−1.51
	Uncovered	130.81	5.46	4.71	−91.98	−26.70	−2.21
Albedo	−10%	102.93	5.62	4.06	−67.50	−25.95	−1.62
	−5%	127.02	5.57	3.66	−58.83	−25.84	−2.21
	+5%	70.08	5.65	2.97	−41.57	−25.17	−1.22
	+10%	61.32	5.60	2.57	−33.26	−24.92	−1.19
	+15%	50.37	5.56	2.27	−25.37	−24.50	−1.05

5.3 Sensitivity to albedo

Results from both model simulations and *in-situ* measurements in covered and uncovered areas corroborate the anticipated outcome that an increase in albedo leads to reduced ablation. To evaluate the mass balance sensitivity to variations in cover albedos, model runs were conducted with albedo parameters adjusted by −10% to +15%. The outcomes from point-model analyses (Fig. 8 and Table 3) demonstrate that alterations in geotextile albedo substantially influence both the glacier surface mass balance and the energy balance. These changes predominantly impact net short-wave radiation and the energy necessary for ablation, more so than other energy components. A 5% enhancement in geotextile albedo leads to a reduction in S_{net} by an average of 10 W m^{-2} per hour and Q_{melt} by an average of 8 W m^{-2} per hour, culminating in a total ablation reduction of 0.20 m w.e. With a 10% and 15% increase in geotextile albedo, S_{net} shows a decreasing trend, accompanied by a reduction in the energy utilized by Q_{melt} to a certain extent, resulting in a total reduction in ablation ranging from 0.35–0.55 m w.e. Conversely, a decrease in geotextile albedo by 10% and 5% leads to reduced reflection of short-wave radiation, thereby increasing S_{net}. This, in turn, escalates the energy consumed by Q_{melt}, weakening the geotextile's protective impact. However, the level of ablation still remains lower than that in the uncovered area, primarily due to the higher albedo of the geotextile compared to the natural ice surface.

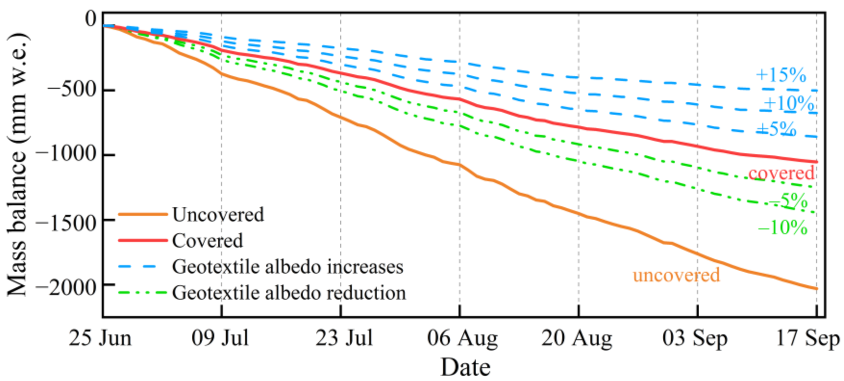

Fig. 8. Short-wave albedo changes on glacier mass balance from 26 June to 17 September, 2023.

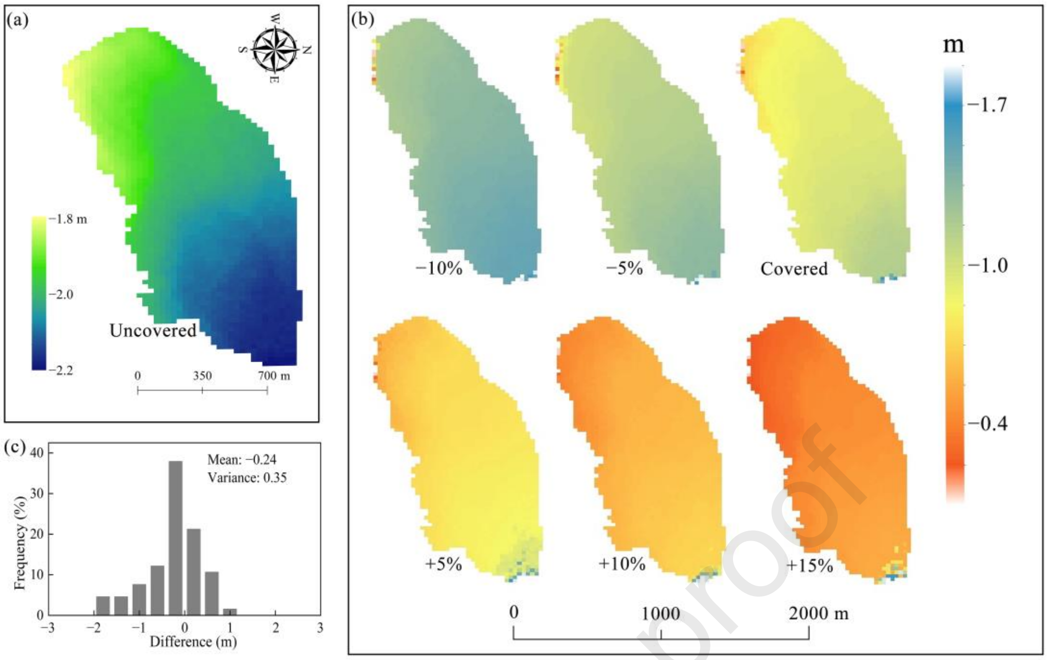

Fig. 9. Distributed mass-balance modeling for various coverage contexts of the BLH from 26 June to 17 September, 2023, (a) natural state, (b) different albedo parameter coverage scenarios, and (c) difference between simulation and UAV measurements.

The distributed mass balance assessments in BLH show that glacier ablation averages about 2.2 m in the terminus areas, with a decrease observed towards the upper parts of the glaciers, as shown in Fig. 9a. The modeled (observed) mean specific ablation within the UAV scanning area is recorded at –2.39 m (–2.15 m). These findings are considered promising, taking into account the model parameterizations and the utilization of a high-resolution DEM derived from UAV data, despite the glacier surface's complex terrain. Additionally, glacier terminal melting is notably more intense, leading to a slightly higher absolute value of elevation change detected by the UAV compared to the simulated value. According to the distributed simulation results, during the testing period from 26 June to 17 September, 2023, glacier ablation in BLH without coverage ranged from 1.8–2.2 m, resulting in an ice volume loss of 2.90×10^6 m^3. Covering the glacier completely with geotextile material reduced glacier ablation to between 0.85–1.13 m, leading to an ice volume loss of 1.45×10^6 m^3. In essence, over a two-month period, complete coverage of the glacier could reduce ice volume loss by up to 50%. Enhancements in the albedo performance of the cover material, such as increases of 5%, 10%, and 15%, lead to further reductions in ablation. As depicted in Fig. 9b, with each 5% increase in the albedo of the cover material, the total ice volume loss is reduced to 1.16×10^6 m^3, 0.89×10^6 m^3, and 0.64×10^6 m^3, corresponding to reductions in ice loss of 60%, 69%, and 78%, respectively. Achieving albedo performance of glacier protection materials exceeding 70% is feasible, not considering cost. Li et al. (2022) demonstrated the efficacy of high albedo radiation-cooled nanomaterials in protecting mountain glaciers. However, this study was limited to establishing a test field at the glacier's terminus and did not extend observations to the middle and upper parts. The distributed model simulation seems to underestimate albedo in the accumulation area and overestimate the mass balance in the upper part of the glacier, underscoring the necessity for future research to provide more comprehensive data supporting glacier protection strategies through coverage. This study focused exclusively on observing and modeling the effects and physical processes of artificial cover on continental glaciers. Given that the Tibetan Plateau, with its extensive glacier coverage, is the largest glacier field outside the polar regions and includes marine glaciers, future research should assess the efficacy of artificial cover in various glaciated regions of the Tibetan Plateau and at different elevations.

5.4 Benefit, impacts and alternatives

The examination of these studies shows the efficacy of using geotextiles to reduce glacier melting rates. The simulation of this experiment indicates that the protective effect of geotextiles is primarily due to their high short-wave albedo. However, previous studies and available data suggest that the short-wave albedo of geotextiles is lower than that of fresh and granular snow (Xie et al., 2023). This paper purposely analyzed the effect of geotextiles with different albedos on glacier ablation, and validate through modeling that regular geotextiles with low albedos will weaken the snow recharge effect during the accumulation period.In addition, the geotextile will also be affected by the environment with time gradually aging, albedo gradually reduced (Fig. 7), and Q_{melt} will increase. The above factors will cause the protection effect to be reduced. Therefore, in practice, geotextiles should ideally be deployed at the beginning of the ablation period and removed at its conclusion (Senese et al., 2020; Huss et al., 2021). Additionally, Fig. 7 illustrates that the albedo of geotextiles decreases over time, reducing their protective effect, and suggests that periodic replacement is necessary for their long-term effectiveness. These measures have been applied in limited areas due to the high costs and labor requirements, restricting their use to areas that are most vulnerable. Ski resorts on glaciers in the European Alps have assessed the expense of glacier conservation against its benefits, resulting in greater investments in glacier coverage in recent period (Fischer et al., 2016). This suggests the viability of employing geotextile coverings for glacier protection in economically feasible locations such as glacier ski resorts or parks. Utilizing geotextiles in glacier settings offers several advantages. For instance, geotextiles can function as insulating barriers, enhancing ice surface reflectivity, decreasing heat absorption, and thus lowering the rates of glacier melting (Olefs and Fisher, 2007). Furthermore, geotextiles, when used on seasonal snow or ice and combined with artificial snow production, can delay the release of meltwater in a manner similar to ice stupas, by postponing meltwater runoff by one to two months, extending into the dry summer season (Nestler et al., 2014).

However, while the mitigation efforts using geotextile coverage show potential for combating glacial retreat, it is critical to evaluate the possible environmental and socio-economic effects of its application. A major concern is the impact on natural glacier dynamics and landscape processes, which could influence downstream water flow, sediment transport, and ecological systems (Huss et al., 2021). Additionally, questions about the long-term durability and environmental impact of geotextiles highlight concerns about their ecological footprint and accumulation in delicate ecosystems (Cauvy-Fraunié and Dangles, 2019). On the social front, deploying geotextile solutions could lead to disputes over resources, land usage, and traditional ways of living, emphasizing the need for thorough engagement with stakeholders and inclusive decision-making processes. Although these effects are expected to be minimal due to the currently limited trials on the Chinese glacier, a broader evaluation of environmental sustainability is warranted if the coverage is extended to the entire glacier or a larger area.

Given the challenges and uncertainties associated with geotextile use, it is crucial to investigate alternative glacier management methods. With the pressing need to address glacier melting due to climate change, prioritizing the reduction of greenhouse gas emissions is essential over finding technological interventions to slow glacier melting (Zheng et al., 2019). Lowering greenhouse gas emissions remains the most effective strategy to curb future atmospheric warming and, consequently, global glacier mass loss. An alternative technological solution to physically covering glaciers is artificial or technological snow production (Oerlemans et al., 2017; Wang et al., 2023), which enhances the glacier's mass balance and surface reflectivity, thereby reducing solar radiation absorption and aiding in glacier preservation, creating a beneficial feedback loop. Large-scale artificial interventions in solar radiation management, such as increasing stratospheric sulfate aerosols or injecting SO_2 into the stratosphere to stabilize the net radiative forcing at the top of the atmosphere, are emerging as promising approaches for reducing glacier melt rates without relying exclusively on geotextile interventions (Zhao et al., 2017).

The mitigation of glacier geotextile coverage represents a promising yet complex approach to addressing the challenges of glacial retreat. Artificial melt reduction may be useful in a clear economic context and on a small scale. In this case, however, the goal is not to protect the glacier as a whole, but to slow down the melting of the targeted area, for example for tourism development (Huss, 2024). While offering potential benefits such as enhanced glacier stability and hydrological regulation, geotextile deployment entails environmental, socio-economic, and ethical considerations that warrant careful scrutiny. Exploring alternative strategies and embracing a holistic, interdisciplinary approach to glacier management are essential for navigating the complexities of climate change adaptation.

6. Conclusion

This study indicates that the geotextile covering the glacier had a greatly effect on slowing the ablation rate. A total of 300 m^2 of geotextile covering the BLH end was found to have slowed the glacier from ablation by nearly 1 m w.e. by approximately 48%, according to field measurements from 26 June to 17 September, 2023.

It was observed that the thickness in the uncovered area decreased by 3 to 2 m, while in the covered area, the thickness change predominantly ranged from –1.5 to −1 m. The COSIPY model effectively conducted single-point and distributed simulations for both the covered and uncovered areas, with the outcomes closely aligning with the observed summer mass balance data. Simulation results indicated that the mass balance in the covered area was –1052 mm w.e. (ablation rate: –12.5 mm w.e. d^{-1}), whereas, in the uncovered area, it was –2029 mm w.e. (ablation rate: –24.2 mm w.e. d^{-1}). S_{net} was the primary source of melt energy in both the covered (80.09 W m^{-2}, 93%) and uncovered (130.81 W m^{-2}, 90%) areas, yet it was greatly lower in the covered areas. This reduction is primarily attributed to the geotextile's high albedo of 0.63%, markedly higher than the glacier surface's albedo of 0.39. Furthermore, a sensitivity study on geotextile albedo revealed that an increase in albedo leads to a decrease in ablation; specifically, for every 5% increase in albedo, ablation was reduced by 10%–25%. Assuming complete coverage of the glacier with geotextile, the glacier's volume loss could be reduced by up to 50%, with every 5% increase in the albedo of geotextile potentially mitigating ice volume loss by approximately 2.5×10^5 m^3.

However, this study is constrained by cost and labor limitations, and experimental observations were not conducted on a larger scale; simulations were restricted to available meteorological parameters. Future research will involve further experiments across various scales, elevations, and seasons, utilizing improved meteorological data. Although geotextiles demonstrate promise for glacier conservation, it is crucial to differentiate between large-scale applications and localized measures. The implications of artificial snow production/augmentation in conjunction with geotextiles for glacier preservation need more detailed examination.

Declaration of competing interest

The authors declare no conflict of interest.

Acknowledgments

This work was supported by the Science and Technology program of Gansu Province (23ZDFA017, 22ZD6FA005), the Third Comprehensive Scientific Expedition of Xinjiang Uyghur Autonmous Region (2022xjkk0802), National Natural Science Foundation of China (42301168), and Gansu Province Science Foundation for Youths (23JRRA673).

References

Ageta, Y., Fujita, K., 2000. Effect of summer accumulation on glacier mass balance on the Tibetan Plateau revealed by mass-balance model. J. Glaciol. 46(153), 244–252. https://doi.org/10.3189/172756500781832945.

Arndt, A., Schneider, C., 2023. Spatial pattern of glacier mass balance sensitivity to atmospheric forcing in High Mountain Asia. J. Glaciol. 1–18. https://doi.org/10.1017/jog.2023.46.

Bhattacharya, A., Bolch, T., Mukherjee, K., et al., 2021. High Mountain Asian glacier response to climate revealed by multi-temporal satellite observations since the 1960s. Nat. Commun. 12(1), 4133. https://doi.org/10.1038/s41467-021-24180-y.

Blau, M., Turton, J., Sauter, T., et al., 2021. Surface mass balance and energy balance of the 79°N Glacier (Nioghalvfjerdsfjorden, NE Greenland) modeled by linking COSIPY and Polar WRF. J. Glaciol. 67, 1–15. https://doi.org/10.1017/jog.2021.56.

Brun, F., Berthier, E., Wagnon, P., et al., 2017. A spatially resolved estimate of High Mountain Asia glacier mass balances from 2000 to 2016. Nat. Geosci. 10(9), 668–673. https://doi.org/10.1038/ngeo2999.

Cauvy-Fraunié, S., Dangles, O., 2019. A global synthesis of biodiversity responses to glacier retreat. Nat. Ecol. Evol. 3(12), 1675–1685. https://doi.org/10.1038/s41559-019-1042-8.

Chen, J., Du, W., Kang, S., et al., 2023. Comparison of energy and mass balance characteristics between two glaciers in adjacent basins in the Qilian Mountains. Clim. Dyn. 61(3), 1535–1550. https://doi.org/10.1007/s00382-022-06641-2.

de Vrese, P., Stacke, T., Caves Rugenstein, J., 2021. Snowfall-albedo feedbacks could have led to deglaciation of snowball Earth starting from mid-latitudes. Commun. Earth Environ. 2(1), 91. https://doi.org/10.1038/s43247-021-00160-4.

Dehecq, A., Gourmelen, N., Gardner, A., et al., 2019. Twenty-first century glacier slowdown driven by mass loss in High Mountain Asia. Nat. Geo. 12(1), 22–27. https://doi.org/10.1038/s41561-018-0271-9.

Farinotti, D., Round, V., Huss, M., et al., 2019. Large hydropower and water-storage potential in future glacier-free basins. Nature 575(7782), 341–344.

https://doi.org/10.1038/s41586-019-1740-z.

Fischer, A., Helfricht, K., Stocker-Waldhuber, M., 2016. Local reduction of decadal glacier thickness loss through mass balance management in ski resorts. Cryosphere 10(6), 2941–2952. https://doi.org/10.5194/tc-10-2941-2016.

Gardner, A., Moholdt, G., Cogley, J., et al., 2013. A reconciled estimate of glacier contributions to sea level rise: 2003 to 2009. Science 340, 852–857. https://doi.org/10.1126/science.1234532.

Hantel, M., Ehrendorfer, M., Haslinger, A., 2000. Climate sensitivity of snow cover duration in Austria. Int. J. Climatol. 20(6), 615–640. https://doi.org/10.1002/(SICI)1097-0088(200005)20:6<615::AID-JOC489>3.0.CO;2-0.

Huss, M., 2024. On the feasibility of glacier preservation. Nat. Water 2(7), 606–607. https://doi.org/10.1038/s44221-024-00269-8.

Huss, M., Hock, R., 2018. Global-scale hydrological response to future glacier mass loss. Nat. Clim. Change 8(2), 135–140. https://doi.org/10.1038/s41558-017-0049-x.

Huss, M., Schwyn, U., Bauder, A., et al., 2021. Quantifying the overall effect of artificial glacier melt reduction in Switzerland, 2005–2019. Cold Reg. Sci. Technol., 184, 103237. https://doi.org/10.1016/j.coldregions.2021.103237.

James, M., Robson, S., Smith, M., 2017. 3-D uncertainty-based topographic change detection with structure-from-motion photogrammetry: precision maps for ground control and directly georeferenced surveys. Earth Surf. Processes Landforms 42, 1769–1788. https://doi.org/10.1002/esp.4125.

Kang, S., Zhang, Y., Qian, Y., et al., 2020. A review of black carbon in snow and ice and its impact on the cryosphere. Earth-Sci. Rev. 210, 103346. https://doi.org/10.1016/j.earscirev.2020.103346.

Li, J., Liang, Y., Li, W., et al., 2022. Protecting ice from melting under sunlight via radiative cooling. Sci. Adv. 8(6), eabj9756. https://doi.org/10.1126/sciadv.abj9756.

Martínez-Carricondo, P., Agüera-Vega, F., Carvajal-Ramírez, F., et al., 2018. Assessment of UAV-photogrammetric mapping accuracy based on variation of ground control points. Int. J. Appl. Earth Obs. Geoinf. 72, 1–10. https://doi.org/10.1016/j.jag.2018.05.015.

Mölg, T., Maussion, F., Yang, W., et al., 2012. The footprint of Asian monsoon dynamics in the mass and energy balance of a Tibetan glacier. Cryosphere 6(6), 1445–1461. https://doi.org/10.5194/tc-6-1445-2012.

Mott, R., Stiperski, I., Nicholson, L., 2020. Spatio-temporal flow variations driving heat exchange processes at a mountain glacier. Cryosphere 14(12), 4699–4718. https://doi.org/10.5194/tc-14-4699-2020.

Naegeli, K., Huss, M., 2017. Sensitivity of mountain glacier mass balance to changes in bare-ice albedo. Ann. Glaciol. 58(75pt2), 119-129. https://doi.org/10.1017/aog.2017.25

Nestler, A., Huss, M., Ambartzumian, R., et al., 2014. Hydrological implications of covering wind-blown snow accumulations with geotextiles on Mount Aragats, Armenia. Geosciences 4(3). https://doi.org/10.3390/geosciences4030073.

Oerlemans, J., Haag, M., Keller, F., 2017. Slowing down the retreat of the Morteratsch glacier, Switzerland, by artificially produced summer snow: a feasibility study. Clim. Change 145(1), 189-203. https://doi.org/10.1007/s10584-017-2102-1.

Olefs, M., Fischer, A., 2008. Comparative study of technical measures to reduce snow and ice ablation in Alpine glacier ski resorts. Cold Reg. Sci. Technol. 52(3), 371–384. https://doi.org/10.1016/j.coldregions.2007.04.021.

Olson, M., Rupper, S., 2019. Impacts of topographic shading on direct solar radiation for valley glaciers in complex topography. Cryosphere 13(1), 29–40. https://doi.org/10.5194/tc-13-29-2019.

Osipov, E.Y., Osipova, O.P., 2021. Surface energy balance of the Sygyktinsky Glacier, south Eastern Siberia, during the ablation period and its sensitivity to meteorological fluctuations. Sci. Rep. 11(1), 21260. https://doi.org/10.1038/s41598-021-00749-x.

Potocki, M., Mayewski, P.A., Matthews, T., et al., 2022. Mt. Everest’s highest glacier is a sentinel for accelerating ice loss. NPJ Clim. Atmos. Sci. 5, 7. https://doi.org/10.1038/s41612-022-00230-0.

Pritchard, H.D., 2019. Asia’s shrinking glaciers protect large populations from drought stress. Nature 569(7758), 649–654. https://doi.org/10.1038/s41586-019-1240-1.

Qiao, G., Yuan, X., Florinsky, I., et al., 2023. Topography reconstruction and evolution analysis of outlet glacier using data from unmanned aerial vehicles in Antarctica. Int. J. Appl. Earth Obs. Geoinf. 117, 103186. https://doi.org/10.1016/j.jag.2023.103186.

Sauter, T., Arndt, A., Schneider, C., 2020. COSIPY v1.3: an open-source coupled snowpack and ice surface energy and mass balance model. Geosci. Model Dev. 13(11), 5645–5662. https://doi.org/10.5194/gmd-13-5645-2020.

Schaefer, M., Fonseca-Gallardo, D., Farías-Barahona, D., et al., 2020. Surface energy fluxes on Chilean glaciers: measurements and models. Cryosphere 14(8), 2545-2565. https://doi.org/10.5194/tc-14-2545-2020.

Senese, A., Azzoni, R. S., Maragno, D., et al., 2020. The non-woven geotextiles as strategies for mitigating the impacts of climate change on glaciers. Cold Reg. Sci. Technol. 173. https://doi.org/10.1016/j.coldregions.2020.103007.

Spandre, P., Morin, S., Lafaysse, M., et al., 2016. Integration of snow management processes into a detailed snowpack model. Cold Reg. Sci. Technol. 125, 48–64. https://doi.org/10.1016/j.coldregions.2016.01.002.

Wang, F., Liu, S., Wang, X., et al., 2023. Geotextile protection of glacier: observed and simulated impacts on energy and mass balance. Adv. Clim. Change Res. 14(6), 963–975. https://doi.org/10.1016/j.accre.2023.11.001.

Wang, F., Yue, X., Wang, L., et al., 2020. Applying artificial snowfall to reduce the melting of the Muz Taw Glacier, Sawir Mountains. Cryosphere 14(8), 2597–2606. https://doi.org/10.5194/tc-14-2597-2020.

Williamson, S. N., Menounos, B., 2021. The influence of forest fire aerosol and air temperature on glacier albedo, western North America. Remote Sens. Environ. 267, 112732. https://doi.org/10.1016/j.rse.2021.112732.

Xie, Y., Wang, F., Xu, C., et al., 2023. Applying artificial cover to reduce melting in Dagu Glacier in the eastern Qinghai–Tibetan Plateau. Remote Sens. 15(7), 1755. https://doi.org/10.3390/rs15071755.

Yang, W., Guo, X., Yao, T., et al., 2011. Summertime surface energy budget and ablation modeling in the ablation zone of a maritime Tibetan glacier. J. Geophys. Res. Atmos. 116(D14). https://doi.org/10.1029/2010JD015183.

Yao, T., Bolch, T., Chen, D., et al., 2022. The imbalance of the Asian water tower. Nat. Rev.

Earth Environ. 3(10), 618–632. https://doi.org/10.1038/s43017-022-00299-4.
Zemp, M., Jansson, P., Holmlund, P., et al., 2010. Reanalysis of multi-temporal aerial images of Storglaciären, Sweden (1959–99): Part 2: comparison of glaciological and volumetric mass balances. Cryosphere 4(3), 345–357. https://doi.org/10.5194/tc-4-345-2010.
Zhang, Y., Gao, T., Kang, S., et al., 2021. Albedo reduction as an important driver for glacier melting in Tibetan Plateau and its surrounding areas. Earth-Sci. Rev. 220, 103735. https://doi.org/10.1016/j.earscirev.2021.103735.
Zhao, C., Yang, W., Miles, E., et al., 2023. Thinning and surface mass balance patterns of two neighbouring debris-covered glaciers in the southeastern Tibetan Plateau. Cryosphere 17(9), 3895–3913. https://doi.org/10.5194/tc-17-3895-2023.
Zhao, H., Su, B., Huajin, L., et al., 2022. A new projection for glacier mass and runoff changes over High Mountain Asia. Science Bulletin 68(1), 43–47. https://doi.org/10.1016/j.scib.2022.12.004.
Zhao, L., Yang, Y., Cheng, W., et al., 2017. Glacier evolution in high-mountain Asia under stratospheric sulfate aerosol injection geoengineering. Atmos. Chem. Phys. 17(11), 6547–6564. https://doi.org/10.5194/acp-17-6547-2017.
Zheng, X., Streimikiene, D., Balezentis, T., et al., 2019. A review of greenhouse gas emission profiles, dynamics, and climate change mitigation efforts across the key climate change players. J. Cleaner Prod. 234, 1113–1133. https://doi.org/10.1016/j.jclepro.2019.06.140.

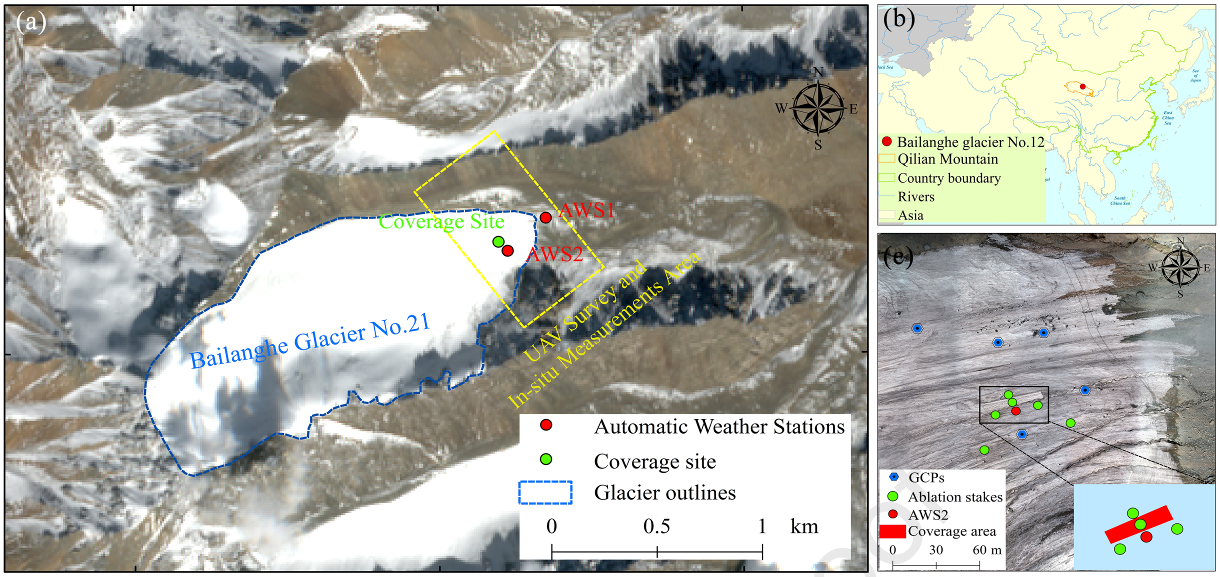
(a)
Coverage Site
AWS1
AWS2
Bailanghe Glacier No.21
UAV Survey and
In-situ Measurements Area
Automatic Weather Stations
Coverage site
Glacier outlines
0
0.5
1
km
(b)
Bailanghe glacier No.12
Qilian Mountain
Country boundary
Rivers
Asia
(c)
GCPs
Ablation stakes
AWS2
Coverage area
0
30
60 m

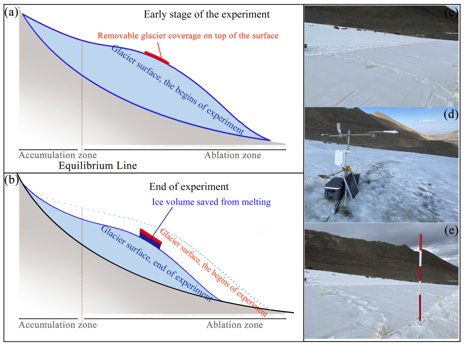
(a)
Early stage of the experiment
Removable glacier coverage on top of the surface
Glacier surface, the begins of experiment
Accumulation zone
Ablation zone
Equilibrium Line
(b)
End of experiment
Ice volume saved from melting
Glacier surface, end of experiment
Glacier surface, the begins of experiment
Accumulation zone
Ablation zone
(d)
(e)

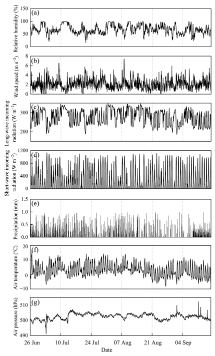

(a)
Relative humidity (%)
(b)
Wind speed (m s^{-2})
(c)
Long-wave incoming radiation (W m^{-2})
(d)
Short-wave incoming radiation (W m^{-2})
(e)
Precipitation (mm)
(f)
Air temperature (°C)
(g)
Air pressure (hPa)
26 Jun
10 Jul
24 Jul
07 Aug
21 Aug
04 Sep
Date

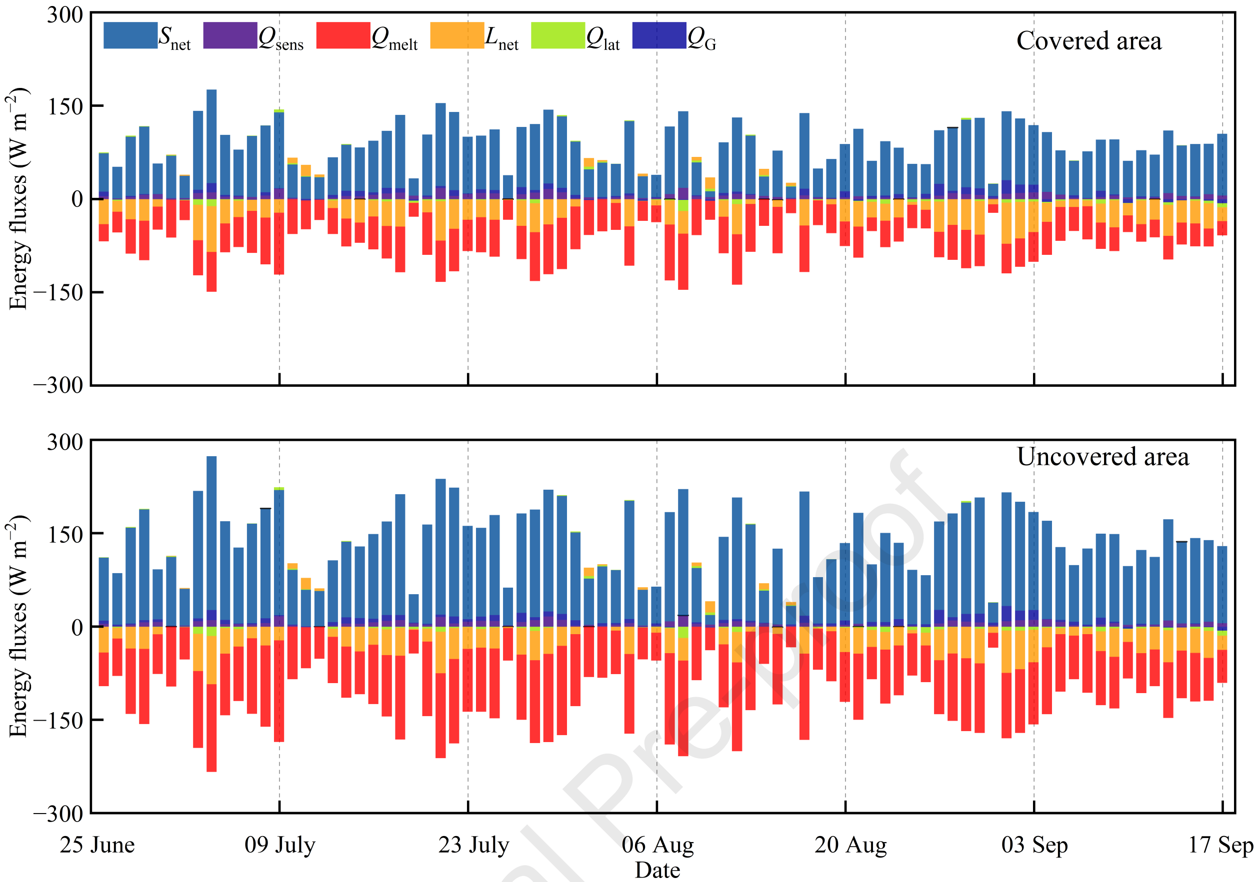

300
150
0
−150
−300
Energy fluxes (W m^{-2})
S_{net}
Q_{sens}
Q_{melt}
L_{net}
Q_{lat}
Q_G
Covered area
Uncovered area
25 June
09 July
23 July
06 Aug
20 Aug
03 Sep
17 Sep
Date

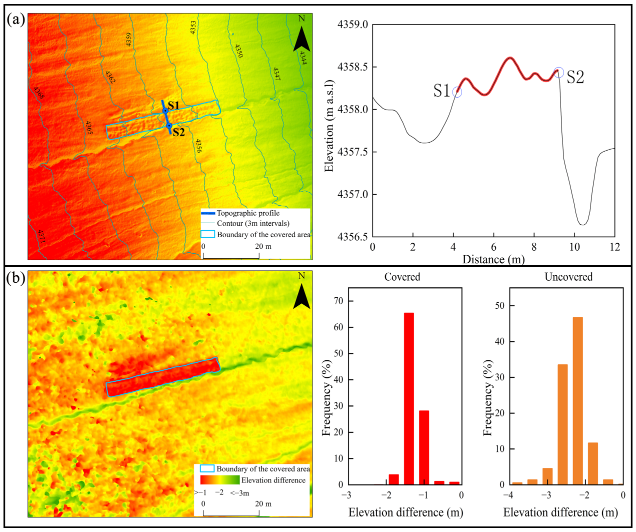
(a)
Topographic profile
Contour (3m intervals)
Boundary of the covered area
20 m
S1
S2
Elevation (m a.s.l)
Distance (m)
(b)
Boundary of the covered area
Elevation difference
Covered
Uncovered
Frequency (%)
Elevation difference (m)

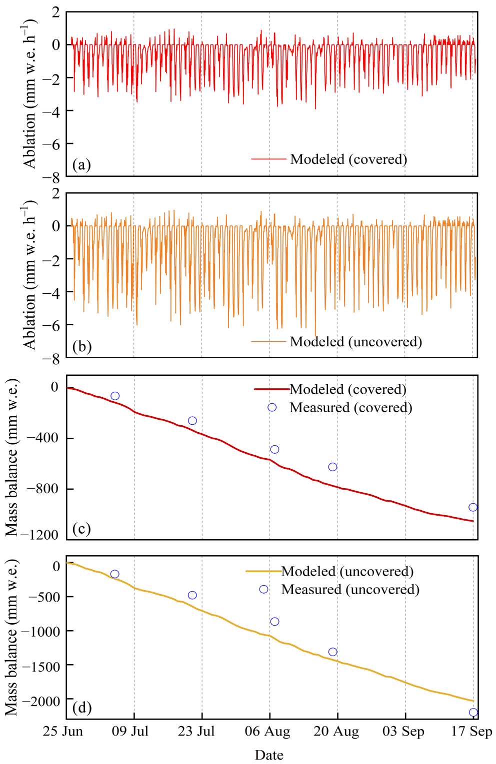

Ablation (mm w.e. h^{-1})
(a)
Modeled (covered)
(b)
Modeled (uncovered)
Mass balance (mm w.e.)
Modeled (covered)
Measured (covered)
(c)
Modeled (uncovered)
Measured (uncovered)
(d)
25 Jun
09 Jul
23 Jul
06 Aug
20 Aug
03 Sep
17 Sep
Date

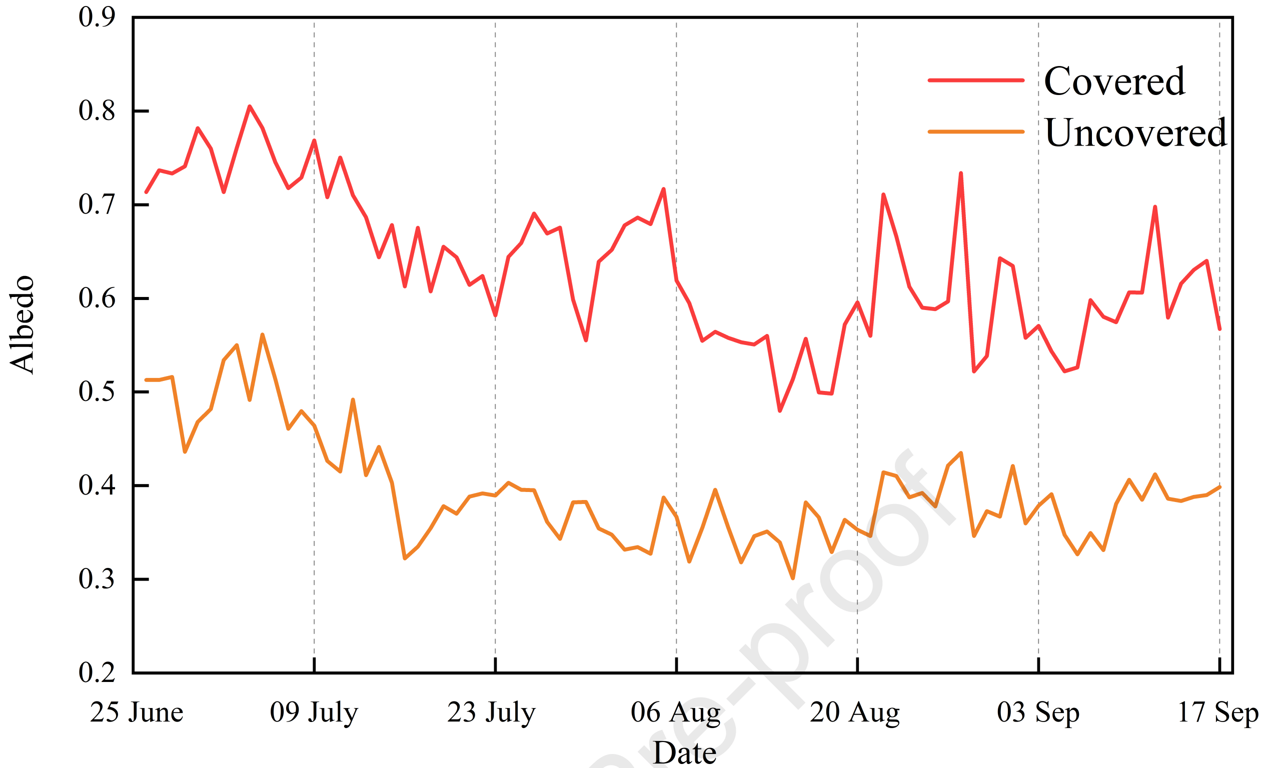
0.9
0.8
0.7
0.6
0.5
0.4
0.3
0.2
Albedo
25 June
09 July
23 July
06 Aug
20 Aug
03 Sep
17 Sep
Date
Covered
Uncovered

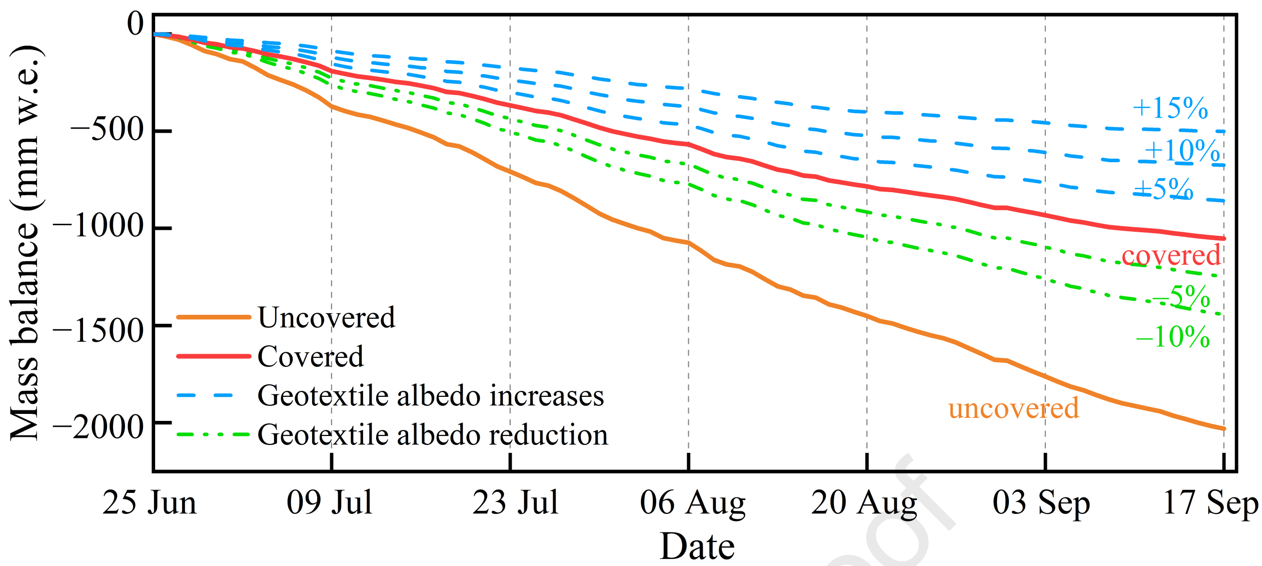
0
−500
−1000
−1500
−2000
Mass balance (mm w.e.)
25 Jun
09 Jul
23 Jul
06 Aug
20 Aug
03 Sep
17 Sep
Date
Uncovered
Covered
Geotextile albedo increases
Geotextile albedo reduction
+15%
+10%
+5%
covered
−5%
−10%
uncovered

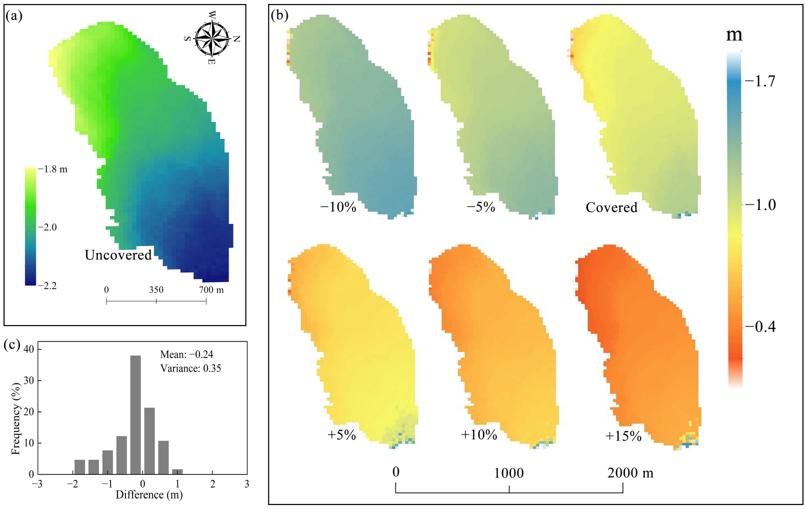
(a)
W
N
S
E
−1.8 m
−2.0
−2.2
Uncovered
0
350
700 m
(b)
−10%
−5%
Covered
+5%
+10%
+15%
m
−1.7
−1.0
−0.4
0
1000
2000 m
(c)
Mean: −0.24
Variance: 0.35
Frequency (%)
Difference (m)